JOURNAL OF CATALYSIS 99, 358–374 (1986)

The Role of Multiparticle–Adatom Interactions on the Sintering of Supported Metal Catalysts

DADY B. DADYBURJOR,*,[1] STEVEN P. MARSH,† AND MARTIN E. GLICKSMAN†

*Department of Chemical Engineering, West Virginia University, Morgantown, West Virginia 26506-6101; and †Materials Engineering Department, Rensselaer Polytechnic Institute, Troy, New York 12181

Received May 14, 1985; revised January 14, 1986

Sintering of supported metal particles involves the transfer of single atoms (adatoms) and the movement of crystallites on the substrate. The present work considers the coupled role of all crystallites in determining the diffusion of adatoms on the two-dimensional surface, and the consequent growth and dissolution of crystallites. A decomposition–summation procedure is used. The results of this approach can be compared to those from the mean-field approach, where multiparticle interactions are neglected. The present approach is particularly valid when metal crystallites are found in clumps on the surface, i.e., at high local metal loadings. The particle size distributions that result when multiparticle interactions are considered in the sintering analysis depend upon the metal loading, and are significantly flatter and broader than those of the "asymptotic" mean-field analysis. Further, the average particle size calculated here increases with metal loading, in contrast to that from the "asymptotic" mean-field analysis. Finally, the relationship between the time of sintering and the average particle size calculated here changes from concave to convex at higher metal loadings. © 1986 Academic Press, Inc.

INTRODUCTION

Sintering of supported metal catalysts refers to the phenomenon by which the average size of the metal crystallites increases with time. This leads to a net loss of exposed metal surface area and therefore a loss of catalytically active sites, i.e., the catalyst is deactivated. The phenomenon is a thermodynamically driven effect, namely the minimization of surface free energy. However, the kinetics of the process are slow enough that equilibrium, represented by a single large metal particle per catalyst pellet, is not achieved.

There are a variety of kinetic processes occurring in parallel during sintering. These include the migration of single atoms (hereinafter, adatoms) through the vapor phase and on the substrate, and the migration of two- or more-atom particles on the substrate. Models for these processes have been discussed and compared in a number of papers and reviews (*1–5*). In this work the emphasis is on an Ostwald ripening model, i.e., one where the migrating entities are restricted to adatoms, and where driving forces for the changes in shape and size arise from differences in chemical potential with particle radii of curvature. A well-known mathematical treatment of Ostwald ripening in three dimensions (3D), i.e., where migration is through the vapor phase, is due to Lifshitz and Slyozov (*6*); whereas Chakraverty (*7*) first treated the phenomenon of adatom migration on the substrate, i.e., two-dimensional (2D) Ostwald ripening. We describe these analyses in somewhat more detail below, because of their relevance to our present work.

In Refs. (*6, 7*), attention is focussed on a single particle at a time, and on its mean interaction with the rest of the system. The concentration of adatoms around the given particle can be described by the vector form of Fick's Law, in spherical coordinates for the 3D case and in cylindrical coordinates

---

[1] To whom inquiries should be addressed.

0021-9517/86 $3.00

for the 2D case. The assumption of thermodynamic equilibrium at the particle interface allows the use of the Gibbs–Thomson equation as a boundary condition. The supersaturation is assumed to be "small," thereby allowing a linearized version of this equation to be used. As another boundary condition, the so-called "mean-field" assumption is used. Accordingly, the adatom concentration reaches its uniform mean value, i.e., its equilibrium value in the bulk single atom phase, at a given distance, the so-called "screening distance," from the particle surface (in 3D) or base (in 2D). The screening distance is proportional to the particle radius, with the proportionality constant of order unity. A schematic representation of the system, 2D for the sake of simplicity, is shown in Fig. 1a. Using this approach, the diffusion flux or rate of size change can be obtained for each individual particle. Consequently, sintering rates for the entire system and rates of change of average size can be obtained from the particle size distribution (PSD), i.e., $n^*(R^*, t^*)$ as a function of R^*. (Here and in what follows we use the superscript asterisk to denote dimensional quantities. For the sake of conciseness, the equations below are written in nondimensional terms, which are represented without the asterisk for the sake of clarity.) Finally, after a certain induction time has passed, the PSD of the system approaches a so-called "asymptotic" value. That is to say, although the absolute PSD continues to change with the passage of time while sintering continues, there is no change with time for an appropriately nondimensional PSD, for which $n^*(R^*, t^*)/n^*_{\max}(t^*)$ is plotted against $R^*/R^*_{\max}(t^*)$. Note that the scaling terms in both axes would change with time.

Such an approach is a useful approximation if the metal particles are sufficiently far apart on the support, i.e., if metal loadings are sufficiently low. Nominal values of metal loadings are of the order of 0.1 wt% metal on the catalyst. For a substrate surface area of 100 m^2/g and an average particle size of 100 Å, this works out to an average of 5500 Å, i.e., more than 50 particle-diameters, between particles. However, electron microscopy of model and real catalysts, for example, see Ref. (*8*), indicates that there are areas where actual distances may be one or more orders of magnitude smaller than the average value. Metal particles are found in clumps on the catalyst surface, and within these clumps the "mean-field" assumptions may not be valid.

Further, Lee (*9*) has noted that the assumption of a "small" supersaturation is

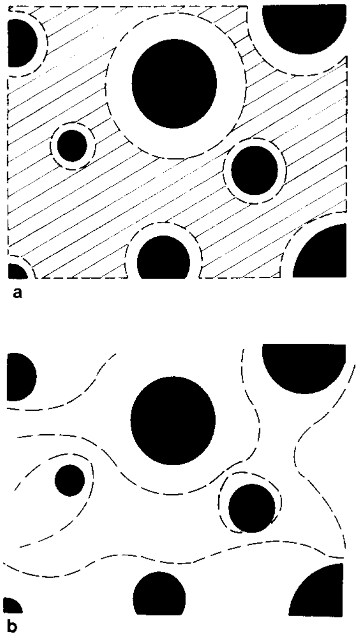

FIG. 1. System of metal particles and adatoms on a substrate, as visualized according to two different analyses. The dark circles represent the particles. (a) the "Mean-Field" Approach. The shaded area is the "Mean-Field" region where the adatom concentration is uniform. The white area around each particle is the region where the concentration increases or decreases, in a radially symmetric manner, to the "Mean-Field" value. Each particle interacts only with the "Mean-Field" region. (b) The Multiple-Particle Effect Approach. There is no shaded area, and the adatom concentration in the white region is not radially symmetric but depends upon the location and size of all the particles. The dashes represent lines of equal adatom concentration. The particles interact with one another through the adatom region.

generally not valid for catalyst systems. Modifying the linearized form of the Gibbs–Thomson equation, to allow for these larger values of the supersaturation, leads to larger values of the adatom concentration around each particle, and faster sintering rates than those predicted by Chakraverty (*7*).

Realistically, each of the ripening particles has a rate of growth that is determined not by its size alone, but is also affected by the relative sizes and locations of all other particles, particularly by the nearby particles. An extreme example of this effect is called "direct ripening" and was treated by Ruckenstein and Dadyburjor for both the 2D (*10*) and the 3D (*11*) case. Here two particles are sufficiently close that a significant portion of their individual screening areas overlap. Then adatoms could move "directly" from the smaller to the larger particle, i.e, without passing through the bulk adatom phase.

A suitable model for sintering rates must take into account the effect on the individual particle of all other particles, notably the closer ones. Qualitatively, these interaction effects can be explained as follows. The particles, by emitting and adsorbing adatoms at their interfaces, influence the availability of the adatoms for other particles. In this manner, each particle affects the growth rates of all the others. This would lead to the prediction of sintering rates that depend upon (local) metal loadings, and conceivably also upon the (initial) position of the particles. A schematic representation of the surface following such a model is shown in Fig. 1b. As in Figure 1a, the representation is restricted to 2D migration for the sake of simplicity. In this case, note that the adatom region of the system is not divided into a screening region and a mean field region, and that adatom concentration profiles are now no longer symmetric around the particles.

The analysis of such a system has been worked out (*12, 13*) for the case of 3D Ostwald ripening, i.e, vapor-phase adatom transport. In that case, the asymptotic PSD is found to depend strongly upon the loading of the system, but not upon the initial positions of the particles. The work described below is a model to describe multiparticle interactions when the transport of adatoms is on the substrate alone, i.e., 2D Ostwald ripening.

ANALYSIS

The model developed in the present work will be comparable to Chakraverty's in that the diffusion is two-dimensional, the particles are assumed to be in the shape of hemispheres, and the Gibbs–Thomson boundary condition is applied. However, the "screening distance" simplification will be avoided since the diffusion field will be calculated directly from the array of interacting particles.

The modeling of a collection of ripening particles on a flat substrate can be simplified by considering each particle as a point source/sink of solute atoms. This equivalent point source/sink is located at the center of the circular base of the particle. The sign convention used for the source/sink strength provides a positive value for a growing particle (sink) and a negative value for a shrinking particle (source). The magnitude of the particle source/sink strength indicates the rate at which it grows or shrinks. The advantage of using these point sources is that the quasistatic diffusion field problem may now be solved as a potential field problem, where the potential represents the dimensionless adatom concentration. This similarity arises because both fields are described by Poisson's equation. For a collection of *N* point sources/sinks on a plane, this equation takes the form

$$\nabla^2 C(\mathbf{r}, t) = \sum_{i=1}^{N} -2\pi B_i(t)\delta[\mathbf{r} - \mathbf{r}_i]. \quad (1a)$$

Here *C* is the nondimensional concentration of adatoms, given by

$$C \equiv (C^* - C_0^*)/C_0^* \quad (1b)$$

r is the nondimensional location of a point on the plane,

$$\mathbf{r} \equiv \mathbf{r}^*/l_c^* \tag{1c}$$

$\mathbf{r}_i$ is the nondimensional location of the center of the ith particle on the plane,

$$\mathbf{r}_i = \mathbf{r}_i^*/l_c^* \tag{1d}$$

and l_c^* is the nondimensionalizing length parameter, to be defined later. B_i is the source/sink strength of the ith particle, which is located at $\mathbf{r}_i$, and δ is the usual Dirac delta function.

Equation (1a) is not valid at $\mathbf{r} = \mathbf{r}_i$ (physically, at the center of any particle) but this restriction is unimportant since the regions near $\mathbf{r} = \mathbf{r}_i$, i.e., inside the particles, are not part of the diffusion field domain. Further, the adatom concentration profile in the system is assumed to vary reasonably slowly with time. Then C can be considered a scalar "potential" in the system, resulting from the contributions of all N sources or sinks. Because of the linear nature of Eq. (1a), a general solution to this equation in two dimensions (and time) is the linear combination of logarithmic terms

$$C(\mathbf{r}, t) = B_0(t) + \sum_{i=1}^{N} B_i(t) \log|\mathbf{r} - \mathbf{r}_i|. \tag{2}$$

Equation (2) is valid everywhere except at $\mathbf{r} = \mathbf{r}_i$. B_0 is a "reference potential" which is non-zero in general. Note that all of the B_i terms (i.e., all of the particles) contribute, albeit to different extents, to the "potential" (the concentration profile of adatoms). Further, the diffusive interaction among particles is now apparent, since B_i values are size- and location-dependent.

Conservation of mass criteria lead to a global closure condition given by

$$\lim_{N\to\infty}\left[\sum_{i=1}^{N} B_i\right] = 0. \tag{3}$$

This can be used as the first of $(N + 1)$ boundary conditions required to solve for the values of B_0 and B_1 through B_N.

The other N boundary conditions are the relations for the adatom concentrations at the interfaces of the N particles, each given by a Gibbs–Thomson-type equation. The familiar form of this equation is

$$C_{pi}^* = C_0^* \exp[2\sigma^* v_m^*/(k^* T^* R_i^*)]. \tag{4a}$$

In nondimensional terms,

$$C_{pi} = \exp[1/R_i] - 1 \tag{4b}$$

where the nondimensional concentration at the perimeter of the ith particle is defined by

$$C_{pi} \equiv (C_{pi}^* - C_0^*)/C_0^* \tag{4c}$$

the nondimensional radius of the ith particle by

$$R_i = R_i^*/l_c^* \tag{4d}$$

and the nondimensionalizing length parameter l_c^* by

$$l_c^* \equiv 2\sigma^* v_m^*/k^* T^*. \tag{4e}$$

Since the diffusion field is no longer radially symmetric around each individual particle, the perimeter adatom concentration is not necessarily constant for a given particle. Hence we can no longer rigorously use Eq. (4b). Instead we apply this relation to the perimeter-averaged concentration $\overline{C}_{pi}$, given by

$$\overline{C}_{pi} \equiv \int C_{pi} d|\mathbf{p}_i|/(2\pi R_i) = \exp[1/R_i] - 1. \tag{5}$$

Here the integral is over the perimeter of the particle base. (Note that the loss of radial symmetry also implies that the particles will no longer remain as perfect hemispheres. We neglect this complication and implicity assume R_i to be the perimeter-averaged radius of the ith particle.)

Equations (2), (3), and (5) in principle allow the adatom concentration $C(\mathbf{r}, t)$ to be evaluated. Graphically, a concentration "contour map," such as that given by the dotted curves in Fig. 1b, can be drawn at any given time. In terms of modeling for sintering phenomenon, however, our interest is more in the values obtained for the source/sink strengths $B_i(t)$, as shown below.

For the ith particle, the volumetric growth rate V_i is given in terms of the diffusion flux $\boldsymbol{J}_i$ as

$$V_i = \int \mathbf{J}_i \cdot d\mathbf{n}_i. \qquad (6)$$

Here the integral is over the perimeter of the particle base. Substituting the dimensionless form of Fick's law

$$\mathbf{J}_i = -\nabla C_i \qquad (7)$$

and using the divergence theorem, yields

$$V_i = 2\pi B_i. \qquad (8a)$$

Further, differentiating the volume of the particle yields

$$V_i = 2\pi(R_i)^2 dR_i/dt. \qquad (8b)$$

Equating the righthand sides of Eqs. (8a, b) yields

$$dR_i/dt = B_i/R_i^2. \qquad (9)$$

Equation (9) yields the rate of change of each of the N particle radii in the system, in terms of the source/sink strength B_i for the particle. The value of B_i is obtained from Eqs. (3) and (5), and therefore depends upon *all* the particles, not just upon the ith particle radius, R_i.

Two problems arise with this treatment. First there is no simple way of determining a suitable number of particles in the system. Even for large values of N, the values obtained for the B_i are found to change as more particles are added. Further, the logarithmic potential is divergent at large distances, thus making it appear from Eq. (2) as if sources far from the point at $\mathbf{r}$ will make increasingly larger contributions to the adatom concentration!

Instead of a term-by-term expansion of Eq. (2), a decomposition–summation procedure is used. Such a procedure has been used by Ewald (*14*) for summing coulombic potentials in an infinite, three-dimensional lattice. Glicksman and Voorhees (*12, 13*) modified this approach to simulate 3D ripening. The single particle potentials in both Refs. (*12, 14*) have a $1/r$ dependence on distance, and are semiconvergent, whereas the present dependence is logarithmic and nonconvergent.

The decomposition–summation procedure requires two steps. First it is assumed that the large but finite number N of irregularly located and sized particles (source/sink terms) in the system can be replaced by a "basis" set of N' irregularly located and sized particles (where $N' \ll N$) and the images of the basis set repeated a doubly infinite number of times in both dimensions. This system is graphically indicated in Fig. 2. Quantitatively, we introduce the nondimensional lattice-translation vector $\boldsymbol{\tau}$, defined as

$$\boldsymbol{\tau} = h a_0 \hat{i} + k a_0 \hat{j}, \qquad (10a)$$

where a_0 is the nondimensional size of the unit cell containing the "basis" set; $\hat{i}, \hat{j}$ are unit vectors; and h, k are integers. When h and k are both set equal to zero, a particle in the basis set is described; when either one of h, k is non-zero (or both are non-zero), the particle is translated in one (or both) directions and is in one of the translated cells. With this approach, the concentration profile of Eq. (2) can be written as

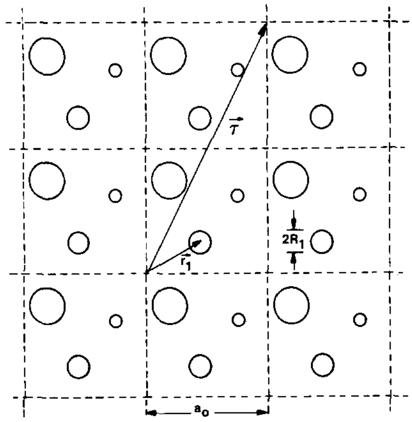

FIG. 2. System of particles consisting of a basis set and some of its infinite translations in two dimensions. For clarity, the basis set is drawn with only three particles in it. The repeating lattice vector $\boldsymbol{\tau}$ drawn corresponds to $h = 1$ and $k = 2$ in Eq. (10a). R_i and $\mathbf{r}_i$ represent the radius and the position vector of the ith particle. The parameter a_0 represents the size of the unit cell.

$$C(\mathbf{r}, t) = B_0(t) + \sum_{\tau} \sum_{j=1}^{N'} B_j(t) \log|\mathbf{r} - (\mathbf{r}_j + \boldsymbol{\tau})| \quad (10b)$$

where the vector sum over $\boldsymbol{\tau}$ is shorthand for summations over both its components, i.e., h and k.

From the physical point of view, the periodicity may be rationalized by noting that, for particles that are sufficiently far away, the contribution of the adatom concentration would depend more upon radial distance than on angular position, and even that dependence is weak. Hence the effect of using an image of one of the N' particles in the basis set, instead of the actual irregularly located particle sufficiently far away, is not noticeable. We return to this later.

The second step in the Ewald decomposition–summation procedure is to replace the point source density distribution, $B_i\, \delta(\mathbf{r}_i)$, for the ith particle (and its translations) by three components. One component contains the point term and a neutralizing Gaussian sink term. The second component contains a Gaussian source term and a neutralizing, spatially uniform, sink. The third term contains a spatially uniform source. The source density distribution and its components are illustrated in Fig. 3, using a one-dimensional system for the sake of simplicity.

The advantage of this formulation is that each of the components can be substituted in Eq. (1), which can then be solved component-by-component for the potential/concentration C. The details are summarized in Appendix I and described in Ref. (*15*), but the results can be seen to be

$$C(\mathbf{r}, t) = B_0(t) + (2\pi/\Delta) \sum_{j=1}^{N'} \sum_{\mathbf{g}}{}' \{(B_j(t)/G^2) \exp[-(G^2\Delta/4\pi) + I\mathbf{g} \cdot (\mathbf{r} - \mathbf{r}_j)]\} + (1/2) \sum_{j=1}^{N'} \sum_{\tau} \{B_j(t) \mathrm{Ei}[-(\pi/\Delta)|\mathbf{r} - (\mathbf{r}_j + \boldsymbol{\tau})|^2]\}. \quad (11a)$$

Here $\mathbf{g}$ is the reciprocal lattice vector relative to the lattice translational vector $\boldsymbol{\tau}$ and is given by

$$\mathbf{g} = (2\pi h/a_0)\hat{i} + (2\pi k/a_0)\hat{j} \quad (11b)$$

where h and k are the indices of $\boldsymbol{\tau}$. Σ' denotes that the summation over the dummy 2D reciprocal lattice vector $\mathbf{g}$ is to exclude $\mathbf{g} = 0$. The components of C in Eq. (11a) consist of summations, just like Eqs. (2) or (10b). But now each of the summations over $\boldsymbol{\tau}$ are rapidly convergent, in contrast to the sum of the logarithms in Eq. (2). Mathematically, this occurs because at large distances, the Gaussian terms in the density distribution tend to neutralize the corresponding point sources, thus eliminating the logarithmic term in the expression for the potential/concentration C.

Equation (11a) contains $(N' + 1)$ unknowns, the coefficients B_i. One relationship between them is the conservation condition. Unlike Eq. (3), the result is not global closure over all N particles in the system, but local closure over the N' particles in the basis set. This can be expressed as

$$\sum_{j=1}^{N'} B_j = 0. \quad (12)$$

The remaining relations are the Gibbs–Thomson equations for each of the N' particles in the basis set. We substitute Eq. (11) appropriately in the perimeter-averaged relation, Eq. (5), as described in Appendix II, to yield

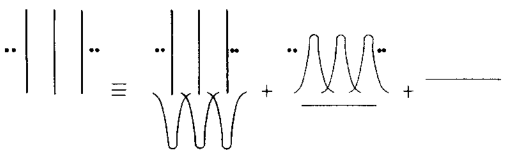

FIG. 3. Decomposition of point source densities following Ewald (*14*). For clarity, only a one-dimensional system is illustrated. The left-hand side consists of a single point source in the basis set and some of its infinite translations. The vertical lines represent delta function sources, the bell-shaped curves are Gaussian sources or sinks, and the horizontal lines represent spatially uniform sources or sinks. Additional point source or sink terms in the basis set, and their translations, can be incorporated by superposition.

$$\exp[1/R_i] - 1 = B_0 + B_i \log R_i + (2\pi/\Delta) \sum_{j=1}^{N'} \sum_{\mathbf{g}}{}' \{(B_j/G^2) \exp[-(G^2\Delta/4\pi) + I\mathbf{g} \cdot \mathbf{r}_{ij}]\} + (1/2) \sum_{j=1}^{N'}{}'' \sum_{\tau} B_j \mathrm{Ei}[-(\pi/\Delta)|\mathbf{r}_{ij} - \boldsymbol{\tau}|^2] + (B_i/2)(\gamma + \log[\pi/\Delta] + \sum_{\tau}{}' \mathrm{Ei}[-(\pi/\Delta)T^2]), \quad (13)$$

where Σ'' denotes that $j = i$ is to be excluded from the summation over j.

Evaluation of the B_i from Eqs. (12) and (13) yields the rate of change in the radius for each of the particles in the basis set, using Eq. (9). Consequently we can predict the sintering behavior of this system of supported metal particles. The values thus obtained reflect the specific size-based interactions among the particles on the support.

The $(N' + 1)$ relations of Eqs. (12) and (13) can be rearranged into a linear system to solve for the B_i coefficients. The matrix form of this system is

$$[\mathrm{Y}] = [\mathrm{A}][\mathrm{B}], \quad (14)$$

where the matrices are defined as follows:

$$[\mathrm{Y}] \equiv \begin{bmatrix} \exp[1/R_1] - 1 \\ \exp[1/R_2] - 1 \\ \vdots \\ \exp[1/R_{N'}] - 1 \\ 0 \end{bmatrix}, \quad (15)$$

$$[\mathrm{B}] \equiv \begin{bmatrix} B_1 \\ B_2 \\ \vdots \\ B_{N'} \\ B_0 \end{bmatrix}, \quad (16)$$

$$[\mathrm{A}] \equiv \begin{bmatrix} D + \log R_1 & A_{12} & \cdots & A_{1N'} & 1 \\ A_{21} & D + \log R_2 & \cdots & A_{2N'} & 1 \\ \vdots & \vdots & \vdots & \vdots & \vdots \\ A_{N'1} & A_{N'2} & \cdots & D + \log R_{N'N'} & 1 \\ 1 & 1 & \cdots & 1 & 0 \end{bmatrix}. \quad (17)$$

The parameter D in the diagonal terms of the [A]-matrix is defined as

$$D \equiv (2\pi/\Delta) \sum_{\mathbf{g}}{}' \{(1/G^2) \exp[-(G^2\Delta/4\pi)]\} + (1/2) \sum_{\tau}{}' \{\mathrm{Ei}[-\pi T^2/\Delta]\} + (1/2)(\gamma + \log[\pi/\Delta]) \quad (18a)$$

and the off-diagonal terms are

$$A_{ij} \equiv (2\pi/\Delta) \sum_{\mathbf{g}}{}' \{(1/G^2) \exp[-(G^2\Delta/4\pi) + I\mathbf{g} \cdot \mathbf{r}_{ij}]\} + (1/2) \sum_{\tau} \{\mathrm{Ei}[-(\pi/\Delta)|\mathbf{r}_{ij} - \boldsymbol{\tau}|^2]\}. \quad (18b)$$

In Eq. (18b), i and j can take on any integer value from 1 to N' such that $i \neq j$.

PROCEDURE

Numerical techniques are used to obtain

the results. Specifications include the initial fractional coverage of the surface by the particles (f_s), the initial PSD, and the number of particles in the basis set (N').

The value chosen for N' represents a compromise between computational convenience (N' particles require inverting a $[N' + 1]$ square matrix equation for each time step) and accuracy (replacing a disordered system with a more ordered one, and approximating a continuous size distribution with a discrete one). Voorhees and Glicksman (*13*) showed that a basis set of 300 particles was adequate for a 3D system of Ostwald ripening; for the two-dimensional system, the actual value used here was closer to $(300)^{2/3}$, i.e., $N' = 50$. It is important to note that the actual system considered contains more than N' particles. Since the basis cell is extended in both directions and both dimensions, we are dealing with a system of fourfold-infinite-N' particles. The value of N' merely specifies the degree of disorder necessary to describe the system adequately, i.e., within the limits of present-day experimental error.

The cell length a_0 is calculated based on the desired surface coverage, N', and initial PSD as

$$a_0 = \left[\pi \sum_{j=1}^{N'} R_j^2/f_s\right]^{1/2}. \qquad (19)$$

The particles are randomly placed in the basis set, care being taken to ensure that there is no overlap of the particles. Based on the initial particle locations and sizes, initial values of the coefficients B_i can be obtained from Eq. (14), rearranged as

$$[\mathrm{B}] = [\mathrm{A}]^{-1}[\mathrm{Y}]. \qquad (20)$$

For each of the N' particles in the basis set, the growth (or decay) rate can be obtained from Eq. (9). For a sufficiently small time interval, the change in (nondimensional) particle radii can be found via

$$R_i(t + \Delta t) - R_i(t) = \{B_i(t)/R_i(t)^2\}\Delta t \quad (21)$$

and this allows the nondimensional radii $R_i(t + \Delta t)$ to be calculated. Based on the new radii, the new values of coefficients B_i are reevaluated from Eq. (20). The procedure is repeated, thus allowing the particle radii to be obtained as functions of (nondimensional) time via repeated applications of Eq. (21). Finally the (nondimensional) surface-area-averaged radius, calculated as

$$\bar{R}(t) \equiv \left\{\sum_{i=1}^{N'} [R_i(t)]^2/N'\right\}^{1/2}, \qquad (22)$$

can be related to time t.

We reiterate here that B_i values depend upon both the location and the size of all particles in the basis set, through the elements of the matrix [A]. Hence, the change in size of each particle is related to the location and size of all of the particles. Hence the sintering behavior of the given system depends upon the location and size of the entire system of particles.

RESULTS

In the present work, values of f_s, the initial fractional coverage of the surface by the metal crystallites, were chosen to range from 10^{-5} to 0.30. This range includes the lower values where the mean-field and small-saturation assumptions could be expected to be valid, and higher values corresponding to both commercial and model supported catalysts. The initial PSD used is shown in the histograph of Fig. 4. It was chosen to approximate the "asymptotic" distribution analytically obtained by Chakraverty (*7*), the idea being that multiparticle effects on the PSD would show up most clearly as a difference from the "mean-field" PSD. The value of the (dimensional) surface-area-averaged radius $\bar{R}^*$ used initially was chosen to be 10.7 nm.

Values of the nondimensionalizing parameters were taken as representative of those for Pt/Al_2O_3. For the length and concentration,

$$l_c^* = 1.2 \times 10^{-9} \text{ m } (\mathit{17}), \qquad (23a)$$

$$C_0^* = 2.2 \times 10^{-6} \text{ mol/m}^2 \ (\mathit{18}). \quad (23b)$$

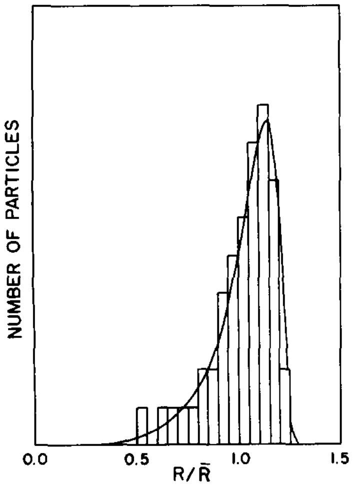

FIG. 4. Histograph of initial particle size distribution used. The curve represents the analytic expression for the "asymptotic" distribution of Chakraverty (7) using the mean-field approximation.

The diffusion coefficient for adatoms, needed to nondimensionalize the time, was taken as

$$D_0^* = 5 \times 10^{-19}\ \mathrm{m^2/s}\ (17). \qquad (23c)$$

Results are illustrated in Figs. 5 through 7. The particle size distributions in Figs. 5 and 6 are normalized following Chakraverty (7). Fig. 5 shows two PSDs after a sintering time of approximately 21 h. The initial distributions for both "runs" of Fig. 5 are identical, and are given by Fig. 4, and both have the same value of $f_s(= 10^{-5})$. However, the N' particles were initially placed in two different random arrangements in the unit cell for the two "runs." The resulting two histograms of Fig. 5 are only marginally different from each other and from that of Fig. 4. This is not surprising, since the initial fractional coverage used in Fig. 5 is small enough for the mean field approximation to be valid, and Fig. 4 represents the asymptotic distribution to be obtained following such an approximation. The surface-area-averaged radii corresponding to the two distributions of Fig. 5 are also similar, approximately 11.0 nm each, and not too far removed from the initial value of 10.7 nm.

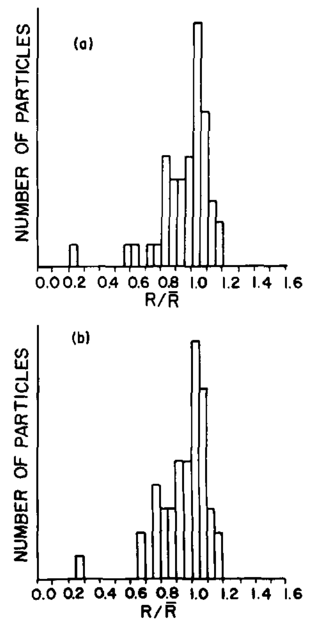

FIG. 5. Histographs of particle size distributions after $t^* = 21$ h of sintering. The initial fractional surface area coverage f_s is 10^{-5}. Graphs (a) and (b) represent two different systems, each with the initial particle size distribution of Fig. 4, but with the particles initially placed in two different random locations in the basis cell.

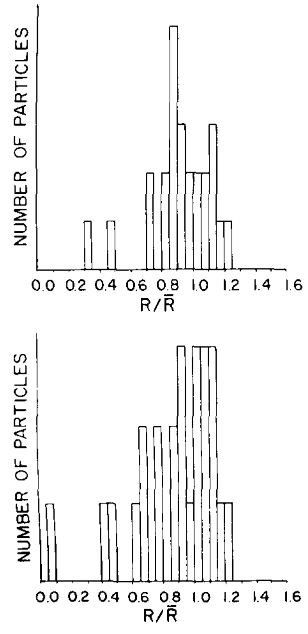

FIG. 6. Same as Fig. 5 except $f_s = 0.30$ and the sintering time is $t^* = 23$ h.

Figure 6 contains histographs corresponding to $f_s = 0.30$ and a sintering time of approximately 23 h. As in Fig. 5, particles were initially placed in the unit cell in two different random arrangements. In contrast to Fig. 5, the resulting histographs of Fig. 6 are appreciably different from the initial one given in Fig. 4, and differ to some extent amongst themselves. The distributions of Fig. 6 in general are considerably broader than the initial one which, it may be recalled, approximated the mean-field asymptotic distribution. Clearly the mean-field approximation is not valid for the large fractional coverage considered here. The average radii corresponding to the histographs of Fig. 6 are 14.0 and 13.7 nm, a difference believed to be not significant. Hence the PSD appears to be more sensitive than the average radius to the initial arrangement of particles in the unit set.

The shape of the histographs in Fig. 6, in particular, are qualitatively different from those expected from the "mean field" analysis leading to Fig. 4. Discontinuities, or bi- and higher-modal distributions can be seen in Fig. 6. Bimodal distributions, and distributions containing a grouping of small particles together with a grouping of much larger particles, have been observed in practice. These observations could not be explained previously. Further, calculations by one of us (*19*) have shown that coverage-dependent "asymptotic" distributions at high values of coverage can be obtained analytically for the case of 3D transport. These distributions exhibit a definite tendency towards bimodality at higher coverages. Although similar coverage-dependent "asymptotic" distributions have not been analytically obtained for our present 2D case, it is reasonable to expect that numerical time-stepping techniques should also show such bimodal distributions.

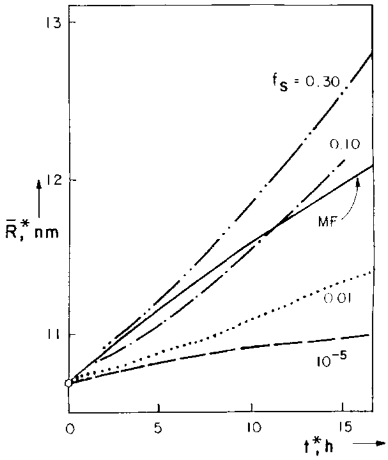

FIG. 7. Surface-area-averaged radii $\bar{R}^*$ as a function of sintering time t^* for different fractional coverages. The continuous curve (MF) represents the time behavior of the radius $R^*_{\max}$, corresponding to the size class with the most particles, expected from the mean-field approximation used by Chakraverty (*7*).

Figure 7 indicates the variation in the (dimensional) average radius, $\bar{R}^*$, with sintering time at various values of the initial fractional coverage, f_s. The continuous line denotes the analytical result from the mean-field approximation of Chakraverty (*7*). The numerical results were printed after every 50 time steps, then joined by a continuous curve. This procedure eliminates the fluctuations caused by using finite values of N'. Values of $\bar{R}^*$ increase monotonically with f_s; this is expected since the closer proximity of particles would increase both sintering rates and the role of multiparticle effects. Further, the shapes of the curves change with f_s. The curves are (initially) convex (with respect to the horizontal axis) for $f_s = 0.10$ and larger values, where multiparticle effects are important. For low values such as $f_s = 10^{-5}$, the curves are (initially) concave. Since values of the fractional coverage decrease during the sintering process (due to the increase in average particle size and to the constant-total-volume constraint), it is clear that at sufficiently long times, all sintering curves are concave. The time required for this transition to occur obviously depends upon the initial fractional coverage, f_s: in the curves labelled $f_s = 0.10$ and 0.30, the transition is not seen in Fig. 7, but the transition may be incipient for the $f_s = 0.001$ curve. For the smallest value of f_s the transition, if it occurs, occurs very early; the entire curve appears concave.

Finally, comparing these curves with the mean-field result, we first note that the shape of the latter is concave, similar to that for small values of f_s. The magnitudes of the "mean-field" values are greater than those for the smallest of f_s values; however, the differences are not significant. The "mean-field" values are actually those of the so-called maximum radius $R^*_{\max}$ (*7*), rather than the surface-area-averaged radius, and the two values differ by about 10%, which is approximately the difference seen here.

SUMMARY AND CONCLUSIONS

Sintering of supported metal catalysts involves the transfer of single atoms and the movement of crystallites on the substrate. The present work neglects crystallite motion, and considers the coupled role of all crystallites in determining the single atom diffusion and the consequent net growth of crystallites. This coupling can be obtained by analogy with the problem of obtaining the potential distribution around a set of point sources and sinks. The decomposition–summation procedure of Ewald allows a rapidly converging summation to be obtained. This is done by adding and subtracting a set of Gaussian sources and a uniformly distributed source. To carry out this summation requires the substitution of the system of particles by a basis set and its translations. The number of particles in the basis set is chosen to be large enough to simulate the essential randomness of the entire system of particles.

The results of this approach can be compared with those from the mean-field approximation, which neglects specific interactions with other particles. Even for the smallest value of the fractional coverage used here, the particle size distribution moves away, at least slightly, from the asymptotic distribution characteristics of the mean-field approximation. This indicates that multiparticle effects may be present even under such conditions. Large values of the fractional coverage lead to a significant flattening of the particle size distribution from the asymptotic mean-field values. Hence it is likely that asymptotic distributions must be evaluated as a function of the fractional coverage using the multiparticle interaction approach.

The average particle sizes computed here can also be compared with the mean-field values. The correspondence with the lowest fractional coverage is good. At higher fractional coverages, the size–time relation changes from concave to convex. It is reasonable to suppose that the convex nature of the curve is a measure of the effect of multiparticle interactions, since the "mean-field" curve is concave.

In conclusion, the present technique is of value in pointing out regions where the simpler "mean-field" analysis may need improvement. Further, the technique quantifies the nature of the multiparticle interactions through the diffusion field, and the corresponding effects on catalyst sintering.

APPENDIX I

Concentration Profile C(r, t) by the Ewald Technique

We start with a quantitative formulation, in 2D, of the three components of the point source/sink density distribution of the jth particle in the "basis" set, $B_j\,\delta(\mathbf{r} - \mathbf{r}_j)$, and its translations:

$$\sum_{\tau} B_j\delta(\mathbf{r} - \{\mathbf{r}_j + \boldsymbol{\tau}\}) = B_j \sum_{\tau} \{\delta(\mathbf{r} - \{\mathbf{r}_j + \boldsymbol{\tau}\}) - (\eta/\pi)\exp[-\eta|\mathbf{r} - (\mathbf{r}_j + \boldsymbol{\tau})^2]\} + \left\{B_j \sum_{\tau} (\eta/\pi)\exp[-\eta|\mathbf{r} - (\mathbf{r}_j + \boldsymbol{\tau})|^2] - B_j/\Delta\right\} + \{B_j/\Delta\}. \quad \text{(I-1)}$$

This relationship was qualitatively illustrated, in one dimension, in Fig. 3. Note that Eq. (I-1) is valid for any value of the Gaussian half-width constant η. Its value will be assigned later, optimized for the maximum rate of convergence in the numerical evaluation of the final expression. Due to the linear nature of the potential (or adatom concentration profile), Poisson's relation (Eq. (1a)) can be separately solved for each of the three contributions of Eq. (I-1) and each of the N' sets of translations plus particle in basis set. The solutions of these subequations can then be summed to give the overall potential (or adatom concentration profile). In this manner we can write

$$C \equiv \sum_{j-1}^{N'} B_j(\psi_{1j} + \psi_{2j} + \psi_{3j}) + (\text{const}). \qquad \text{(I-2)}$$

Here ψ_{1j}, ψ_{2j}, and ψ_{3j} are the solutions of

$$\nabla^2\psi_{\alpha j} = -2\pi\rho_{\alpha j}, \quad \alpha = 1, 2, 3, \qquad \text{(I-3)}$$

where the $\rho_{\alpha j}$ are the contributions to the density distribution of the jth particle in the basis set plus reflections, and are given by

$$\rho_{1j}(\mathbf{r}) \equiv \sum_{\tau} \delta(\mathbf{r} - \{\mathbf{r}_j + \boldsymbol{\tau}\}) - (\eta/\pi) \exp[-\eta|\mathbf{r} - (\mathbf{r}_j + \boldsymbol{\tau})|^2] \qquad \text{(I-4a)}$$

$$\rho_{2j}(\mathbf{r}) \equiv \sum_{\tau} (\eta/\pi) \exp[-\eta|\mathbf{r} - (\mathbf{r}_j + \boldsymbol{\tau})|^2] - (1/\Delta) \qquad \text{(I-4b)}$$

$$\rho_{3j}(\mathbf{r}) \equiv 1/\Delta. \qquad \text{(I-4c)}$$

We now solve Eq. (I-3) for the contribution ψ_{1j}. For any arbitrary source density ρ, we note that the corresponding potential ψ at any point $(\mathbf{r})$ is given by the sum of the contribution to ρ at all points $(\mathbf{r}')$ in 2D space weighted by the logarithm of the distance between the two points, i.e.,

$$\psi(\mathbf{r}) = \int \rho(\mathbf{r}') \log|\mathbf{r} - \mathbf{r}'|d\mathbf{r}'. \qquad \text{(I-5)}$$

This follows from the identity

$$\nabla^2 \log|\mathbf{r}| \equiv -2\pi\, \delta(\mathbf{r}). \qquad \text{(I-6)}$$

Substituting ρ_{1j} into Eq. (I-5) yields, after integration over all space $(\mathbf{r}')$,

$$\psi_{1j} = (1/2) \sum_{\tau} \text{Ei}[-\eta|\mathbf{r} - (\mathbf{r}_j + \boldsymbol{\tau})|^2]. \qquad \text{(I-7)}$$

For the second contribution ψ_{2j}, we note that the Gaussian term in ρ_{2j}, the corresponding density distribution, can be expanded in a general 2D Fourier series with periodicity equal to the dimension of the unit cell, a_0. Then

$$\rho_{2j}(\mathbf{r}) = \sum_{\mathbf{g}} C_{\mathbf{g}} \exp[I\mathbf{g} \cdot (\mathbf{r} - \mathbf{r}_j)] - (1/\Delta), \qquad \text{(I-8)}$$

where $\mathbf{g}$ is the reciprocal lattice vector relative to the lattice translation vector $\boldsymbol{\tau}$ and is given by Eq. (11b). The Fourier coefficients $C_{\mathbf{g}}$ are obtained from the orthogonality relation

$$C_{\mathbf{g}} = (1/\Delta) \int_{(\text{unit cell})} (\eta/\pi) \sum_{\tau} \exp[-\eta|\mathbf{r} - (\mathbf{r}_j + \boldsymbol{\tau})|^2 - I\mathbf{g} \cdot (\mathbf{r} - \mathbf{r}_j)]d\mathbf{r}. \qquad \text{(I-9)}$$

Changing the order of integration and summation leads to an integral over all space, rather than over the single unit cell. Integrating the result yields

$$C_{\mathbf{g}} = (1/\Delta) \exp[-G^2/4\eta]. \qquad \text{(I-10)}$$

Substituting for $C_{\mathbf{g}}$ in Eq. (I-8), we note that the term corresponding to $\mathbf{g} = 0$ in the summation cancels out the $(1/\Delta)$ term. Then

$$\rho_{2j}(\mathbf{r}) = (1/\Delta) \sum_{\mathbf{g}}{}' \exp[-(G^2/4\eta) + (I\mathbf{g} \cdot (\mathbf{r} - \mathbf{r}_j))]. \qquad \text{(I-11)}$$

Substituting this in Poisson's relation, Eq. (I-3), yields

$$\psi_{2j} = (2\pi/\Delta)\, \Sigma'\, (1/G^2) \exp[-(G^2/4\eta) + (I\mathbf{g} \cdot (\mathbf{r} - \mathbf{r}_j))]. \qquad \text{(I-12)}$$

The third contribution to the density, ρ_{3j}, is a uniform source. The corresponding contribution to the potential, ψ_{3j}, will be a constant value. This will only alter the (const) term in Eq. (I-2), or equivalently the B_0 term in Eq. (11) of the text, and B_0 must be determined from the $(N' + 1)$ boundary conditions. (The analogous physical argument is that the adatom concentration is uniform in the absence of metal particles, and that uniform value is obtained from specific initial conditions.) Hence we can set

$$\psi_{3j} = 0 \qquad \text{(I-13)}$$

without loss of generality.

From Eqs. (I-2), (7), (12), (13) we get

$$C = B_0 + (2\pi/\Delta) \sum_{j=1}^{N'} {\sum_{\mathbf{g}}}' \{(B_j/G^2) \exp[-(G^2/4\eta) + I\mathbf{g} \cdot (\mathbf{r} - \mathbf{r}_j)]\} + (1/2) \sum_{j-1}^{N'} \sum_{\boldsymbol{\tau}} \{B_j \operatorname{Ei}[-\eta|\mathbf{r} - (\mathbf{r}_j + \boldsymbol{\tau})|^2]\}. \qquad \text{(I-14)}$$

It now remains to select an optimum value of the Gaussian constant η, related to the half-width of the Gaussian distributions. It can be seen that large values of η increase the exponential factor in the second term of Eq. (I-14). This means that this term will approach convergence with more summations required over **g** as values of η are increased. On the other hand, large values of η result in smaller values of the exponential integral (Ei) factor in the final term of Eq. (I-14). Hence increasing η means that this term will converge requiring fewer summations over $\boldsymbol{\tau}$. The optimum value of η is therefore an intermediate one that will allow rapid convergence of both summation terms in Eq. (I-14). We extrapolate from the work of Tosi (*16*) and determine that

$$\eta = \pi/a_0^2 \qquad \text{(I-15)}$$

is sufficiently close to the optimum value to be useful for our present purposes. We illustrate the reasonableness of this assertion by considering values of

$$C_G \equiv (2\pi/G^2\Delta) \exp[-G^2/4\eta] = \langle 2\pi(h^2 + k^2)\rangle^{-1} \exp[-\pi^2(h^2 + k^2)/(\eta a_0^2)] \qquad \text{(I-16)}$$

and

$$C_L \equiv -(1/2) \operatorname{Ei}[-\eta|\boldsymbol{\tau}|^2] = -(1/2) \operatorname{Ei}[-\eta a_0^2(h^2 + k^2)], \qquad \text{(I-17)}$$

for a range of values of η around (π/a_0^2). Only the first few values of $(h^2 + k^2)$ are used, since both C_G and C_L diminish rapidly for the larger values. The results are shown in Table 1. The smaller values of η result in $C_G < C_L$, and values of C_G drop off faster than do those of C_L when $(h^2 + k^2)$ is increased. The largest value of η results in $C_G > C_L$, and values of C_L drop off faster than those of C_L. At π/a_0^2 we have $C_G \approx C_L$, and both values drop off at about the same rate with increasing values of $(h^2 + k^2)$. These observations confirm our earlier assertion that both series are rapidly convergent for *any* value of η (certainly an improvement over the divergent logarithmic series of Eq. (2) in the text), but that the optimum value of η is close to (π/a_0^2).

Substituting this value in Eq. (I-14) results in the form of the adatom concentration profile shown in Eq. (11) of the text.

APPENDIX II

Evaluation of the Source/Sink Strength Coefficients B_i

We manipulate the (perimeter-averaged) Gibbs–Thomson relations, as given in Eq. (5) of the text, to a form which makes explicit the N' relationships between the coefficients $B_0, B_1, \ldots, B_{N'}$. The most convenient way is first to substitute into Eq. (5)

TABLE 1

C_G and C_L for Various Values of η

$h^2 + k^2$	$\eta = 2/a_0^2$	C_G, C_L $3/a_0^2$	π/a_0^2	$4/a_0^2$
1	1.1 (−3),2.4(−2)	5.9(−3),6.5(−3)	6.9(−3),5.3(−3)	1.4(−2),1.9(−3)
2	4.1 (−6),1.9(−3)	1.1(−4),1.8(−4)	1.5(−4),1.3(−4)	5.7(−4),1.9(−5)
4	1.1(−10),1.9(−5)	7.6(−8),2.4(−7)	1.4(−7),1.3(−7)	2.1(−6),3.3(−9)

the concentration relation of Eq. (2), with the position vector **r** set at points $\mathbf{r}_{\mathrm{p}i}$ on the perimeter of the ith particle:

$$\exp[1/R_i] - 1 = (1/2\pi R_i) \int_{(\text{perimeter})} \Big\{ B_0 + B_i \log R_i + \sum_{\substack{j=1 \\ j \neq i}}^{N} B_j \log|\mathbf{r}_{\mathrm{p}i} - \mathbf{r}_j| \Big\} d|\mathbf{P}_i|. \tag{II-1}$$

Note that the term when $j = i$ has been separated from the others in the summation. Clearly the first two terms in the integral are constant, and therefore are unaffected by averaging over the perimeter. The last term is harmonic and analytic everywhere (unless a point on the perimeter of the ith particle also lies at the center of another particle—an impossible situation since particles are postulated not to touch one another); hence the Poisson integral formula allows the integral around the perimeter to be replaced by the average value at the center. Consequently we can write

$$\exp[1/R_i] - 1 = B_0 + B_i \log R_i + \sum_{\substack{j=1 \\ j \neq i}}^{N} B_j \log|\mathbf{r}_{ij}|. \tag{II-2}$$

We are now faced with a summation of logarithms, with which we expect to have the same difficulties as we had with Eq. (2) of the text. An Ewald treatment is then expected to be useful. Considering the right-hand sides of Eqs. (2) and (11), we can write (approximately) analogous exponential and exponential-integral summation terms for the logarithmic summation of Eq. (II-2), except that **r** is replaced by $\mathbf{r}_i$. The analogy is incomplete because of the exclusion in Eq. (II-2) of $j = i$ from the summation over N particles in the system. The Ewald summation terms must therefore exclude the ith particle from the summation over the N' particles in the basis set, but the *images* of the ith particle in the translated cells *must be included*. Then

$$\exp[1/R_i] - 1 = B_0 + B_i \log R_i + \sum_{j=1}^{N'}{}'' \Big\{ (2\pi/\Delta) \sum_{\mathbf{g}}{}' (B_j/G^2) \exp[-(G^2\Delta/4\pi) + I\mathbf{g} \cdot \mathbf{r}_{ij}] + (1/2) \sum_{\boldsymbol{\tau}} B_j \,\mathrm{Ei}[-(\pi/\Delta)|\mathbf{r}_{ij} - \boldsymbol{\tau}|^2] \Big\} + \{B_i(\psi_{1i}(\mathbf{r}_i) + \psi_{2i}(\mathbf{r}_i) + \psi_{3i}(\mathbf{r}_i))\} - \{B_i \psi_i(\mathbf{r}_i)\}. \tag{II-3}$$

Here the first set of brackets contains terms for the N' particles (*and* their images) excluding the ith particle (*and* its images); the double prime on the summation implies that i is excluded from the summation over j. The second set of brackets contains terms for the ith particle and its images (see Eq. [I-2]), and the last set of brackets subtracts the contribution of the ith particle itself (*without* its images).

From Eqs. (I-8), (10), (11) the contribution from the ith particle and its images, with **r** replaced by $\mathbf{r}_i$, is

$$B_i(\psi_{1i} + \psi_{2i} + \psi_{3i}) = (2\pi/\Delta) \sum_{\mathbf{g}}{}' (B_i/G^2) \exp[-G^2\Delta/4\pi] + (1/2) \sum_{\tau} B_i \,\mathrm{Ei}[-\pi T^2/\Delta]. \tag{II-4}$$

Finally for the ith particle (*without* its images), the density distribution ρ_i' is, from Eq. (I-1)

$$\rho_i'(\mathbf{r}) = \{\delta(\mathbf{r} - \mathbf{r}_i) - (1/\Delta) \exp[-(\pi/\Delta)|\mathbf{r} - \mathbf{r}_i|^2]\} + \{(1/\Delta) \exp[-(\pi/\Delta)|\mathbf{r} - \mathbf{r}_i|^2] - (1/\Delta)\}, \tag{II-5}$$

where the third (constant source) term is ignored as in Appendix I. From Eq. (I-5), this yields the potential at $\mathbf{r} = \mathbf{r}_i$

$$\psi_i'(\mathbf{r}_i) = (1/2)\,\mathrm{Ei}[0] + (1/2)(\gamma + \log[\pi/\Delta]). \tag{II-6}$$

Then Eqs. (II-3), (4), (6) result in

$$
\begin{aligned}
\exp[1/R_i] - 1 &= B_0 + B_i \log R_i \\
&+ \sum_{j=1}^{N'}{}'' \Big\{(2\pi/\Delta) \sum_{\mathbf{g}}{}' (B_j/G^2) \exp[-(G^2\Delta/4\pi) \\
&\quad + I\mathbf{g}\cdot\mathbf{r}_{ij}] + (1/2) \sum_{\boldsymbol{\tau}} B_j \operatorname{Ei}[-(\pi/\Delta)|\mathbf{r}_{ij} \\
&\quad - \boldsymbol{\tau}|^2]\Big\} + B_i(2\pi/\Delta) \sum_{\mathbf{g}}{}' \{(1/G^2) \\
&\quad \exp[-G^2\Delta/4\pi]\} + (B_i/2) \Big\{\gamma + \log[\pi/\Delta] \\
&\quad + \sum_{\boldsymbol{\tau}}{}' \operatorname{Ei}[-\pi T^2/\Delta]\Big\}. \qquad \text{(II-7)}
\end{aligned}
$$

This can be arranged to the form of Eq. (13) in the text.

APPENDIX III: NOMENCLATURE

[A]	particle interaction matrix, Eq. (17)
A_{ij}	off-diagonal element of [A]
a_0	nondimensional length parameter of unit cell containing the basis set, Fig. 2 and Eq. (19)
[B]	particle strength matrix, Eq. (16)
B_i	source/sink strength of *i*th particle, Eq. (1)
B_0	reference potential, or average adatom concentration, Eq. (2)
C^*	adatom concentration at a point on 2D surface
C	nondimensional adatom concentration, Eq. (1b)
$C_{\mathbf{g}}$	Fourier coefficients in adatom concentration profile, Eqs. (I-8), (I-10)
C_{G}, C_{L}	factors in adatom concentration that depend on η, Eqs. (I-16), (17)
C_0^*	adatom concentration in equilibrium with infinitely large particle (flat interface); nondimensionalizing concentration, Eq. (4)
$C_{\mathrm{p}i}^*$	adatom concentration at perimeter $\mathbf{r}_{\mathrm{p}i}^*$
$C_{\mathrm{p}i}$	nondimensional perimeter concentration, Eq. (4c)
$\bar{C}_{\mathrm{p}i}$	average nondimensional perimeter concentration, Eq. (5)
D	parameter in diagonal element of [A], Eq. (18a)
D_0^*	diffusion coefficient of adatoms on 2D surface
$\operatorname{Ei}[x]$	exponential integral function, $\equiv -\int_{-x}^{\infty} (\exp[-t]/t)dt$
f_{s}	initial fractional coverage of 2D surface by particles
$\mathbf{g}$	nondimensional reciprocal lattice vector in 2D for $\boldsymbol{\tau}$, Eq. (11b)
G	magnitude of $\mathbf{g}$, $= \lvert\mathbf{g}\rvert$
h, k	indices for $\boldsymbol{\tau}$, Eq. (10a)
$\hat{i}$, $\hat{j}$	2D unit vectors
I	imaginary operator, $(-1)^{1/2}$
$\mathbf{J}_i^*$	diffusion flux to *i*th particle
$\mathbf{J}_i$	nondimensional flux, $\equiv \mathbf{J}_i^* l_{\mathrm{c}}^*/(C_0^* D_0^*)$, Eq. (7)
k^*	Boltzmann constant
l_{c}^*	nondimensionalizing length parameter, Eq. (4e)
$n^*(R^*, t^*)$	number of particles of radius R^* at time t^*
$n_{\max}^*(t^*)$	number of particles corresponding to $R_{\max}^*$ at time t^*
$\mathbf{n}_i^*$	vector normal to points on interface of *i*th particle
$\mathbf{n}_i$	nondimensional normal vector, $\equiv \mathbf{n}_i^*/l_{\mathrm{c}}^*$
N	number of particles in system, Eq. (1)
N'	number of particles in basis set, Eq. (10b)
$\mathbf{p}_i^*$	vector tangent to points on interface of *i*th particle
$\mathbf{p}_i$	nondimensional tangent vector, $\equiv \mathbf{p}_i^*/l_{\mathrm{c}}^*$
$\mathbf{r}^*$	location of point in system
$\mathbf{r}$	nondimensional location vector, Eq. (1c)
$\mathbf{r}_i^*$	location of center of *i*th particle

$\mathbf{r}_i$	nondimensional particle location, Eq. (1d)
$\mathbf{r}_{ij}^*$	location of center of ith particle relative to the location of the center of the jth particle, $\equiv \mathbf{r}_i^* - \mathbf{r}_j^*$
$\mathbf{r}_{ij}$	nondimensional relative position vector, $\equiv \mathbf{r}_{ij}^*/l_c^*$
$\mathbf{r}_{pi}^*$	location of a point on the perimeter of the ith particle
$\mathbf{r}_{pi}$	nondimensional perimeter location, $\equiv \mathbf{r}_{pi}^*/l_c^*$
R_i^*	radius of ith particle
R_i	nondimensional particle radius, Eq. (4d)
$R_{\max}^*(t^*)$	size of particles present in the greatest number in a PSD at time t^*
$\bar{R}^*$	surface-area-averaged particle radius, $\equiv \bar{R}l_c^*$
$\bar{R}$	nondimensional surface-area-averaged particle radius, Eq. (22)
t^*	time
t	nondimensional time, $\equiv t^*D_0^*/l_c^{*2}$
T^*	absolute temperature
T	magnitude of $\boldsymbol{\tau}$, $\equiv \lvert\boldsymbol{\tau}\rvert$
v_m^*	molar volume of particle
V_i^*	volumetric growth rate of ith particle
V_i	nondimensional growth rate, $\equiv V_i^*/(l_c^*D_0^*)$
[Y]	particle interface matrix, Eq. (15)

Greek

γ	Euler constant, $= 0.577\ldots$
$\delta[x]$	Dirac delta function; $= 0$ if $x \neq 0$, $\int \delta dx = 1$
Δ	nondimensional area of unit cell, $\equiv a_0^2$
∇	nondimensional "dell" operator, $\equiv l_c^*\nabla^*$
η	Gaussian constant, related to half-width of Gaussian distribution, Eqs. (I-1), (I-15)
π	$= 3.14\ldots$
ρ_i'	density distribution due to ith particle in basis set (*without* its images)
ρ_j	density distribution due to jth particle in basis set (*and* its images)
$\rho_{1j}, \rho_{2j}, \rho_{3j}$	contributions to density distribution, ρ_j, Eq. (I-4).
σ^*	particle–substrate interfacial tension
Σ_j'	summation omitting $j = 0$
Σ_j''	summation omitting $j = i$
$\boldsymbol{\tau}$	nondimensional lattice translation vector, Eq. (10a)
ψ_i', ψ_j	potentials due to ρ_i', ρ_j
$\psi_{1j}, \psi_{2j}, \psi_{3j}$	contributions to the potential (ψ_j) that correspond to ρ_{1j}, ρ_{2j}, ρ_{3j}, Eq. (I-3)

ACKNOWLEDGMENT

Partial support of this work by the National Science Foundation under Grants CPE-8320400 and DMR83-08052 is gratefully acknowledged.

REFERENCES

1. Ruckenstein, E., and Dadyburjor, D. B., *Rev. Chem. Eng.* **1,** 251 (1983).
2. Flynn, P. C., and Wanke, S. E., *J. Catal.* **34,** 390, 400 (1974).
3. Wynblatt, P., and Gjostein, N. A., *Acta Metall.* **24,** 1165 (1976).
4. Ruckenstein, E., and Dadyburjor, D. B., *J. Catal.* **48,** 73(1977).
5. Pulvermacher, B., and Ruckenstein, E., *J. Catal.* **35,** 115 (1974).
6. Lifshitz, I. M., and Slyozov, V. V., *J. Phys. Chem. Solids* **19,** 35 (1961).
7. Chakraverty, B. K., *J. Phys. Chem. Solids* **28,** 2401 (1967).
8. Baker, R. T. K., Prestridge, E. G., and Garten, R. L., *J. Catal.* **59,** 293 (1979).
9. Lee, H. H., *J. Catal.* **62,** 129 (1980).
10. Ruckenstein, E., and Dadyburjor, D. B., *Thin Solid Films* **55,** 89 (1978).
11. Dadyburjor, D. B., and Ruckenstein, E., *J. Cryst. Growth* **38,** 285 (1977).
12. Voorhees, P. W., and Glicksman, M. E., *Acta Metall.* **32,** 2001 (1984).
13. Voorhees, P. W., and Glicksman, M. E., *Acta Metall.* **32,** 2013 (1984).

14. Ewald, P., *Ann. Phys. (Leipzig)* **64,** 253 (1921).
15. Marsh, S. P., M. S. thesis, RPI, Troy, New York, 1984.
16. Tosi, P., *in* "Solid State Physics" (F. Seitz and D. Turnbull, Eds.), Vol. 16, p. 1. Academic, New York, 1964.
17. Ruckenstein, E., and Dadyburjor, D. B., *J. Catal.* **48,** 73 (1977).
18. Yao, H. C., Sieg, M., and Plummer, H. K., Jr., *J. Catal.* **59,** 365 (1979).
19. Voorhees, P. W., and Glicksman, M. E., *Metall. Trans. A* **15,** 1081 (1984).